4-2015

Study of EMIC wave excitation using direct ion measurements

Kyungguk Min
Auburn University Main Campus

Kaijun Liu
Auburn University Main Campus

J. Bonnell
University of California - Berkeley

Aaron W. Breneman
University of Minnesota - Twin Cities

Richard E. Denton
Dartmouth College

See next page for additional authors

Recommended Citation

Min, K., et al. (2015), Study of EMIC wave excitation using direction measurements, J. Geophys. Res. Space Physics, 120, 2702–2719, doi:10.1002/2014JA020717.

Authors

Kyungguk Min, Kaijun Liu, J. Bonnell, Aaron W. Breneman, Richard E. Denton, H. O. Funsten, Joerg-Micha Jahn, C A. Kletzing, W. S. Kurth, B. A. Larsen, Geoffrey Reeves, Harlan E. Spence, and J. R. Wygant

RESEARCH ARTICLE

Key Points:
- Study of EMIC wave excitation using directly measured ion measurements
- Integrated analysis of observation, linear theory, and hybrid simulations

Supporting Information:
- Readme
- Data Set S1
- Data Set S2
- Data Set S3
- Data Set S4

Correspondence to:
K. Min,
kmin@auburn.edu

Study of EMIC wave excitation using direct ion measurements

Kyungguk Min[1], Kaijun Liu[1], John W. Bonnell[2], Aaron W. Breneman[3], Richard E. Denton[4], Herbert O. Funsten[5], Jöerg-Micha Jahn[6], Craig A. Kletzing[7], William S. Kurth[7], Brian A. Larsen[5], Geoffrey D. Reeves[5], Harlan E. Spence[8], and John R. Wygant[3]

[1]Department of Physics, Auburn University, Auburn, Alabama, USA, [2]Space Sciences Laboratory, University of California, Berkeley, California, USA, [3]School of Physics and Astronomy, University of Minnesota, Twin Cities, Minneapolis, Minnesota, USA, [4]Department of Physics and Astronomy, Dartmouth College, Hanover, New Hampshire, USA, [5]Los Alamos National Laboratory, Los Alamos, New Mexico, USA, [6]Southwest Research Institute, Space Science Department, San Antonio, Texas, USA, [7]Department of Physics and Astronomy, University of Iowa, Iowa City, Iowa, USA, [8]Institute for the Study of Earth, Oceans, and Space, University of New Hampshire, Durham, New Hampshire, USA

Abstract With data from Van Allen Probes, we investigate electromagnetic ion cyclotron (EMIC) wave excitation using simultaneously observed ion distributions. Strong He band waves occurred while the spacecraft was moving through an enhanced density region. We extract from helium, oxygen, proton, and electron mass spectrometer measurement the velocity distributions of warm heavy ions as well as anisotropic energetic protons that drive wave growth through the ion cyclotron instability. Fitting the measured ion fluxes to multiple $\sin^m$-type distribution functions, we find that the observed ions make up about 15% of the total ions, but about 85% of them are still missing. By making legitimate estimates of the unseen cold (below ~ 2 eV) ion composition from cutoff frequencies suggested by the observed wave spectrum, a series of linear instability analyses and hybrid simulations are carried out. The simulated waves generally vary as predicted by linear theory. They are more sensitive to the cold O+ concentration than the cold He+ concentration. Increasing the cold O+ concentration weakens the He band waves but enhances the O band waves. Finally, the exact cold ion composition is suggested to be in a range when the simulated wave spectrum best matches the observed one.

1. Introduction

Electromagnetic ion cyclotron (EMIC) waves are an integral component of the magnetospheric plasma within the Earth's magnetosphere [e.g., *Thorne et al.*, 2006] and are suggested, at times, to be the dominant contributor to rapid radiation belt electron loss [e.g., *Bortnik et al.*, 2006; *Millan and Thorne*, 2007; *Shprits et al.*, 2013]. It is generally believed that EMIC waves are excited near the magnetic equator through the ion cyclotron instability driven by the anisotropic distribution of energetic ring current ions of tens of keV [e.g., *Cornwall*, 1965] in a frequency range roughly given by $\omega/\Omega_i < A_i/(1 + A_i)$ [*Kennel and Petschek*, 1966], where ω is the wave frequency, Ω_i is the ion gyrofrequency and $A_i = T_{i\perp}/T_{i\parallel} - 1$ is the ion temperature anisotropy ($\perp$ and $\parallel$ denote directions perpendicular and parallel to the background magnetic field, respectively). Theoretical models for the wave excitation indicate that the equatorial region along the high-density duskside plasmapause [*Horne and Thorne*, 1993, 1994; *Jordanova et al.*, 2001; *Chen et al.*, 2010, 2014] is a preferred region for proton cyclotron instability due to the decrease of the energy needed for protons to cyclotron resonate with the waves [e.g., *Cornwall et al.*, 1970; *Perraut et al.*, 1976] and wave guiding by strong-density gradients associated with the plasmapause [*Thorne and Horne*, 1993, 1997]. A series of recent hybrid simulations in the dipole magnetic field [*Hu and Denton*, 2009; *Hu et al.*, 2010; *Omidi et al.*, 2013; *Denton et al.*, 2014] confirmed the major aspects of EMIC wave characteristics, namely, propagation, polarization change, heavy ion effects on wave damping, and wave tunneling through the stop bands.

The presence of heavy ions (He+ and O+) in the magnetosphere complicates wave excitation and propagation characteristics [e.g., *Gomberoff and Neira*, 1983; *Kozyra et al.*, 1984; *Horne and Thorne*, 1994, 1997; *Khazanov et al.*, 2006]. Consequently, the waves are generated in three distinct frequency bands separated by two stop bands immediately above Ω_{He+} and Ω_{O+}, where Ω_{He+} and Ω_{O+} are the helium and oxygen ion gyrofrequencies, respectively. Recent studies showed that sufficiently hot He+ ions can significantly modify the EMIC wave dispersion relation at the frequency near Ω_{He+} [*Chen et al.*, 2011; *Silin et al.*, 2011],

and the resulting wave number as the wave frequency approaches Ω_{He+} cannot be infinitely large. The immediate consequence of this result is that these waves may not be so effective in pitch angle scattering relatively low energy ($\leq$ 2 MeV), geophysically more interesting, relativistic radiation belt electrons as the cold plasma dispersion would otherwise allow.

Gary et al. [2012] further investigated the effect of thermal He+ ions on the EMIC wave excitation in a proton-helium-electron plasma and found that the maximum growth rate of the He band is enhanced by increasing the ratio of helium to proton temperatures parallel to the background magnetic field ($T_{\|He+}/T_{\|H+}$) and by decreasing parallel proton plasma beta ($\beta_{\|H+}$) and He+ concentration, and the maximum unstable wave number on the He band increases with decreasing $T_{\|He+}/T_{\|H+}$ and with increasing He+ concentration. They concluded that He+ ions much cooler than the protons and sufficiently dense are required to grow He band waves at wavelengths considerably shorter than the unstable waves of the proton cyclotron branch, favoring loss of radiation belt electrons of $\leq$ 2 MeV.

Recognizing the importance of realistic multi-ion distributions in understanding the EMIC wave excitation, the present paper attempts to determine the ion distributions based on the direct ion measurements from the Van Allen Probes when EMIC waves were simultaneously observed. The complete measurements of multi-ion species have been difficult, although there are special circumstances in which the background cold ions may directly be detected [*Lee et al.*, 2012; *Lee and Angelopoulos*, 2014]. The direct measurement of heavy ion distributions requires the instrument capable of measuring multi-ion species as low as $\sim$ eV. At the same time, the dominant populations that often have low temperature cannot overcome spacecraft potential induced by charging to be detected by the instrument sensors [*Denton*, 2006].

We present one EMIC wave event observed by the Van Allen Probes, where strong He band waves occurred in the high-density structure presumably within the plume [*Goldstein et al.*, 2014a, 2014b], extract the simultaneously measured ion velocity distributions, and examine wave excitation under this realistic plasma condition by carrying out linear instability analyses and hybrid simulations. A similar event has been recently reported by *Zhang et al.* [2014]. While these authors provided insights into spatiotemporal properties of the observed waves and underlying plasma conditions by utilizing multiple twin-spacecraft orbits and the linear theory testing [*Gary and Lee*, 1994; *MacDonald et al.*, 2008; *Blum et al.*, 2009, 2012], our goal here is to closely examine the excitation of the waves in the observed space plasma environment at a specific moment. Consequently, we are concerned with a shorter time scale and put more effort into the detailed analysis of ion measurements. Following a brief description of the instrument and the event in section 2, analysis of ion distributions, instability analyses, and hybrid simulations are presented in sections 3–5, respectively. Section 6 discusses limitations of the study, and section 7 summarizes the results.

2. Observations
2.1. Instrumentation
The Van Allen Probes spacecraft, the identical twin spacecraft, were launched in late August 2012 into an orbital configuration of 1.1×5.8 R_E that precesses once every other year and are equipped with a suite of state-of-the-art particle and wave experiments [*Mauk et al.*, 2012] that provide data to better understand how populations of relativistic electrons and penetrating ions in space form or change in response to variable inputs of energy from the Sun [*Mauk et al.*, 2012; *Kessel et al.*, 2012].

The Electric and Magnetic Field Instrument and Integrated Science (EMFISIS) instrumentation suite provides measurements of a comprehensive set of wave electric and magnetic fields covering the frequency range from $\sim$10 Hz up to 12 kHz as well as dc magnetic fields with the sampling cadence of 64 vectors/s [*Kletzing et al.*, 2013]. The basic data returned from the wave instrument is a set of spectral matrices including the autocorrelations and cross correlations between the sensors. Additionally in burst mode, full-digitized waveforms from all six sensors are telemetered to enable detailed wave analyses to be performed on the ground. The wave instrument also measures a single electric field component of waves from 10 kHz to 400 kHz in order to determine the spectrum of electron cyclotron harmonic emissions and the frequency of the upper hybrid resonance line which can provide an accurate determination of the electron density. In this paper, high-frequency wave spectra and fluxgate magnetometer data are used to derive the total electron density and EMIC wave power spectra, respectively.

The Electric Fields and Waves (EFW) Instruments, consisting of two pairs of spherical double probe sensors in the spin plane and the third pair deployed at the ends of two stacer booms along the spin axis, are
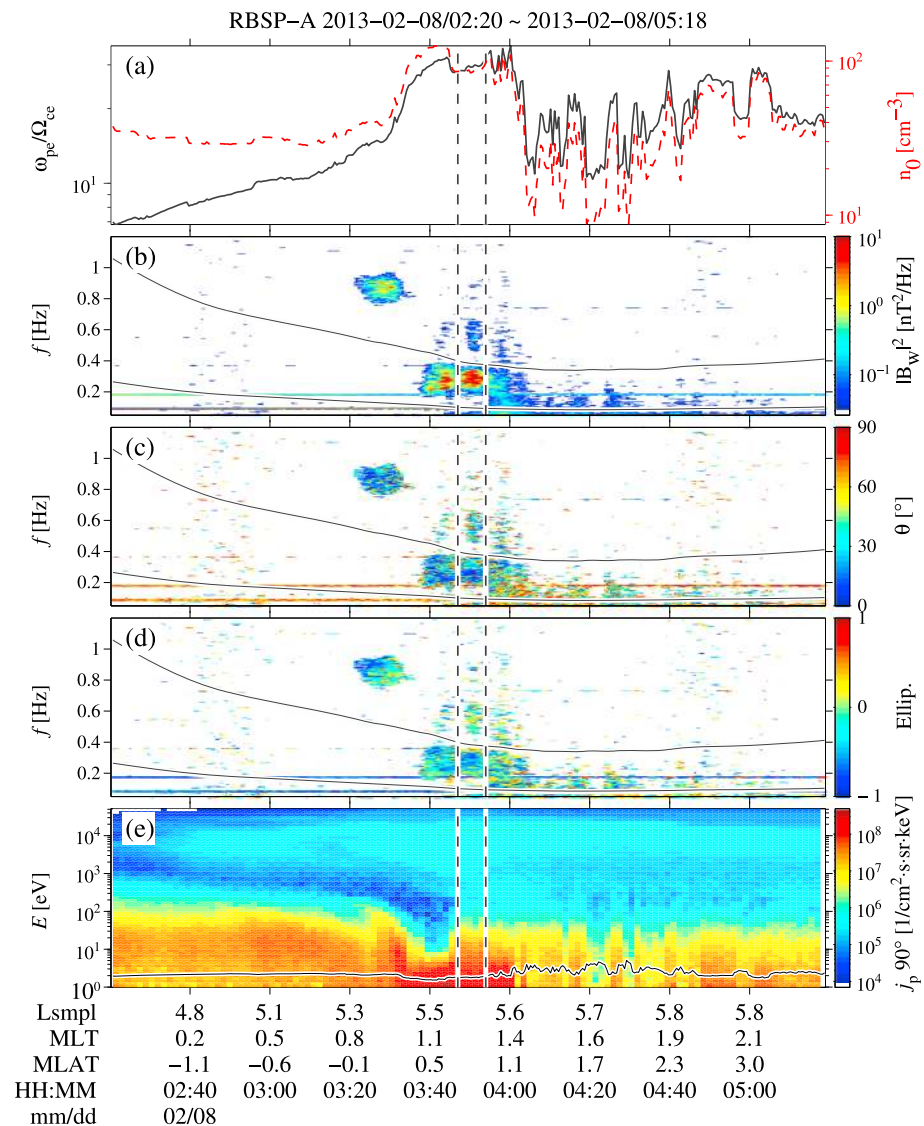
Figure 1. Event overview. (a) Line plots of the plasma density n_0 (dashed curve) and plasma to cyclotron frequency ratio ω_{pe}/Ω_{ce} (solid curve). (b) Total magnetic field wave power. (c and d) Wave normal angle θ and wave ellipticity. (e) 90° H+ differential fluxes. The two solid curves in Figures 1b–1d represent helium and oxygen cyclotron frequencies, respectively. The solid curve in Figure 1e represents the spacecraft potential in units of V. The vertical dashed lines mark the interval (03:47–03:54 UT) analyzed in detail.

designed to measure three-dimensional quasi-static and low-frequency electric fields [*Wygant et al.*, 2013]. Particularly, the instrument provides a continuous stream of measurements of the electric field and spacecraft potential at 32 samples/s in a survey mode. The spacecraft potential measurement is used to correct energies of the ion measurements.

Helium, oxygen, proton, and electron (HOPE) mass spectrometer, one of three pairs of instruments of energetic particle, composition, and thermal plasma (ECT) suite [*Spence et al.*, 2013], is designed to measure the full 3-D in situ plasma ion and electron fluxes [*Funsten et al.*, 2013]. Angular measurements are derived using five angular pixels coplanar with the spacecraft spin axis, and azimuthal measurements are derived using the spacecraft spins (period of ∼12 s) divided into 16 sectors. The instrument discriminates the dominant ion species (H+, He+, and O+), and both ions and electrons are acquired over 1 eV to 50 keV. The instrument is designed to minimize and, if necessary, correct for the background induced by penetrating particles in the harsh environment of the radiation belts. In this study, the Level 3, pitch angle-resolved data product is used.
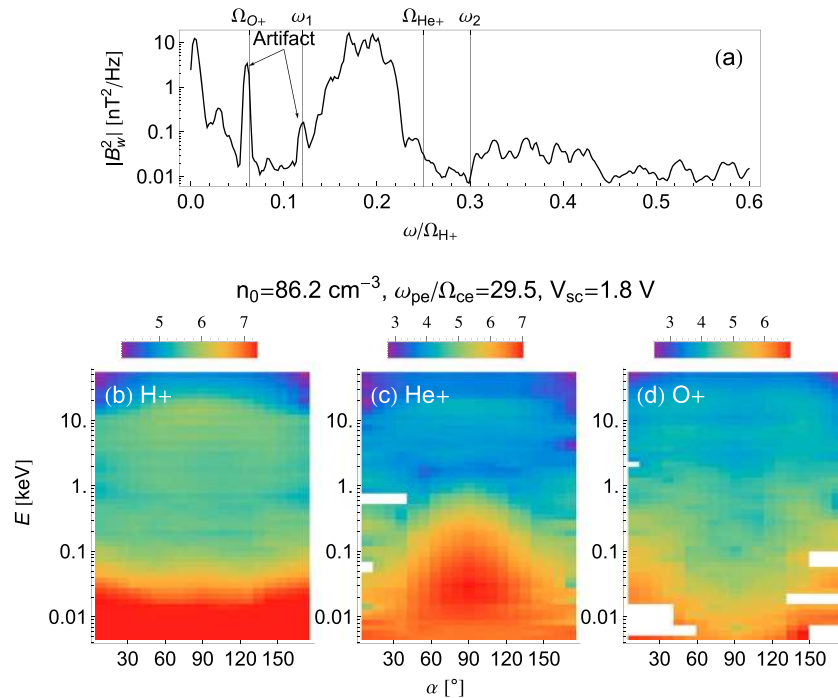
Figure 2. (a) Time-averaged magnetic field wave power spectra. The strongest power occurs in the He band. The small bump between 0.3 and $0.45\Omega_{H+}$ is due to the weak H band waves. The two narrow peaks indicated by the arrows are nonphysical. The lower frequency limits below which the wave power decreases below the noise level are roughly at $0.12\Omega_{H+}$ and $0.3\Omega_{H+}$ denoted by ω_1 and ω_2, respectively. (b–d) From left to right, H+, He+, and O+ fluxes as a function of pitch angle and energy. The color palettes represent logarithmic fluxes in units of cm^{-2} s^{-1} sr^{-1} keV^{-1}. White patches represent missing fluxes at those bins. These fluxes are averaged between 03:46:23 UT and 03:54:01 UT. The color scale of the H+ flux is saturated for energy below ~ 30 eV to enhance contrast of the flux of energetic protons.

2.2. Event Overview

Figure 1 displays an overview of the EMIC wave event closely examined in this study. The waves were observed on 8 February 2013 by the Van Allen Probes-A (Van Allen Probes-B did not see these waves). There was weak storm activity ($Dst \sim -30$ nT) associated with the enhanced solar wind density and southward interplanetary magnetic field at early noon of 7 February, but the activity was very quiet within ± 6 h of the event. The spacecraft was located near the magnetic equator (magnetic latitude $\sim 1°$) at midnight and moved through a density structure, perhaps within the wrapped, residual plume [*Goldstein et al.*, 2014a, 2014b], where the density varied almost by a factor of 2 (Figure 1a, red dashed curve). Fluxes of energetic protons ($E > 1$ keV; Figure 1d) were enhanced since 0220 UT (probably of the plasma sheet origin) and a sudden transition was seen after 0340 UT. H band and He band waves occurred in the regions of $\omega_{pe}/\Omega_{ce} \approx 15$ and $\omega_{pe}/\Omega_{ce} \approx 30$ (Figures 1a and 1b), respectively, where ω_{pe} is the electron plasma frequency estimated from the upper hybrid resonant frequency and Ω_{ce} is the electron gyrofrequency calculated using the background magnetic field. We surmise that the density fluctuations are associated with the enhancement of the EMIC waves at different frequencies as several studies have previously examined [*Thorne and Horne*, 1994; *Chen et al.*, 2009]. Minimum variance analysis [*Santolík et al.*, 2003] confirms that both H and He band waves are strongly left-hand polarized and have wave normal angle of $\sim 20°$ or less (Figures 1c and 1d). Figure 1e presents proton fluxes at pitch angle of 90°, where thermal and hot fluxes were enhanced when the H- and He band waves occurred. The solid curve near the bottom axis represents the spacecraft potential which was low at ~ 2 V throughout the period. In the rest of the paper the strongest He band waves and the associated ion distributions between the two vertical dashed lines, from 03:47 UT to 03:54 UT, are closely examined.

3. Ion Distributions

Figure 2a presents the time-averaged magnetic field wave power spectrum during the interval of interest. The waves in He band are strongest and have a peak roughly at $0.18\Omega_{H+}$, where Ω_{H+} is proton

gyrofrequency. The small bump between $0.3\Omega_{H+}$ and $0.45\Omega_{H+}$ indicates weak H band waves, also seen in Figure 1b. The spikes denoted by the arrows are the interference lines in the magnetic field data and are nonphysical artifacts. Figures 2b–2d present time-averaged H+, He+, and O+ differential fluxes. H+ fluxes are roughly made of two components, one with isotropic and/or butterfly-like thermal component below 100 eV and the other hot, tenuous anisotropic component above 1 keV. He+ fluxes have a very anisotropic thermal component between 10 eV and 1 keV, probably due to perpendicular heating by the EMIC waves observed [e.g., *Anderson and Fuselier*, 1994; *Zhang et al.*, 2010; *Omidi et al.*, 2010]. There also exists a hot, tenuous anisotropic component above 1 keV. O+ fluxes are relatively low, have several missing bins at low energies, and the distribution is butterfly like (to be more precise, inverted "W" shape) across the entire energy channels.

After many experiments and inspired by the loss cone distribution [*Ashour-Abdalla and Kennel*, 1978], multiple $\sin^m$-type distributions of the form

$$
\begin{aligned}
f &= \frac{f_v}{C_v} \times \frac{f_u}{C_u}, \\
f_v &= e^{-v^2/\theta^2}, \\
C_v &= \frac{\pi^{3/2}}{2}\theta^3,
\end{aligned}
\tag{1}
$$

$$
\begin{aligned}
f_u &= (1-\Delta) + \left(\Delta - \frac{1-\Delta}{1-\beta}\right)(1-u^2)^N + \frac{1-\Delta}{1-\beta}(1-u^2)^{\beta N} \text{ for } \beta \neq 1, \\
C_u &= 2(1-\Delta) + \sqrt{\pi}\left(\Delta - \frac{1-\Delta}{1-\beta}\right)\frac{\Gamma(1+N)}{\Gamma(3/2+N)} + \sqrt{\pi}\frac{1-\Delta}{1-\beta}\frac{\Gamma(1+\beta N)}{\Gamma(3/2+\beta N)},
\end{aligned}
\tag{2}
$$

are used to fit the observed ion fluxes, where Γ is the gamma function, v is the total particle speed, $u = \cos\alpha$ (α being pitch angle), θ is the radial thermal speed, $N \geq 0$ is the anisotropy index, and $\beta \geq 0$ and $0 \leq \Delta \leq 1$ determine the shape of pitch angle distribution—N determines the degree of anisotropy, Δ determines whether the distribution is pancake like or butterfly like, and β determines the width of loss cone (Figure 3). C_v and C_u are normalization factors so that $\int_v d^3v f = 1$. In addition, $f_u \geq 0$ is ensured. One may be able to derive an alternative form of f_u for $\beta = 1$ where f_u is singular, but to avoid unnecessary complexity in the fitting process, we make sure that β does not become exactly unity by adding a small number to β. When converted to differential fluxes (that is, $j = Ef$), the magnitude has the form $j_v \propto e^{-E/T}E/T$ which has a local maximum at $E = T$, where $E = mv^2/2$ and $T = m\theta^2/2$. Using

$$
\{\tau_\parallel, \tau_\perp\}(N) \equiv \int_{-1}^{1} du(1-u^2)^N \{\cos^2, \sin^2\}(\alpha) = \sqrt{\pi}\frac{\Gamma(\{1,2\}+N)}{\{2,1\}\times\Gamma(5/2+N)},
$$

the parallel and perpendicular temperatures of the velocity distribution of equation (1) can be written as

$$
\frac{T_\parallel}{m} = \frac{3\theta^2}{2C_u}\left[(1-\Delta)\frac{2}{3} + \left(\Delta - \frac{1-\Delta}{1-\beta}\right)\tau_\parallel(N) + \frac{1-\Delta}{1-\beta}\tau_\parallel(\beta N)\right] \text{ and}
\tag{3}
$$

$$
\frac{T_\perp}{m} = \frac{3\theta^2}{4C_u}\left[(1-\Delta)\frac{4}{3} + \left(\Delta - \frac{1-\Delta}{1-\beta}\right)\tau_\perp(N) + \frac{1-\Delta}{1-\beta}\tau_\perp(\beta N)\right],
\tag{4}
$$

respectively.

Equation (1) has been used as the base distribution function to fit the observed ion fluxes for the following reasons. First, with only three free parameters (N, Δ, and β), the f_u function can represent rich variety of observed particle distributions, namely, isotropic, pancake-like, butterfly-like distributions and more, as illustrated in Figure 3. Second, such richness has an added advantage when the data have several missing bins, and the distribution can still be deduced based upon the overall shape that best fits the existing bins. Third, despite many terms involved in equation (1), the fitting is not as difficult as it appears (for example, compared to fitting with multiple loss cone distributions). This is because the energy and pitch angle-dependent terms in equation (1) are already separated as are the observed fluxes. Finally, once the analytic representation is obtained, the parallel and perpendicular temperatures equivalent to those of the bi-Maxwellian distribution can be easily retrieved using equations (3) and (4).
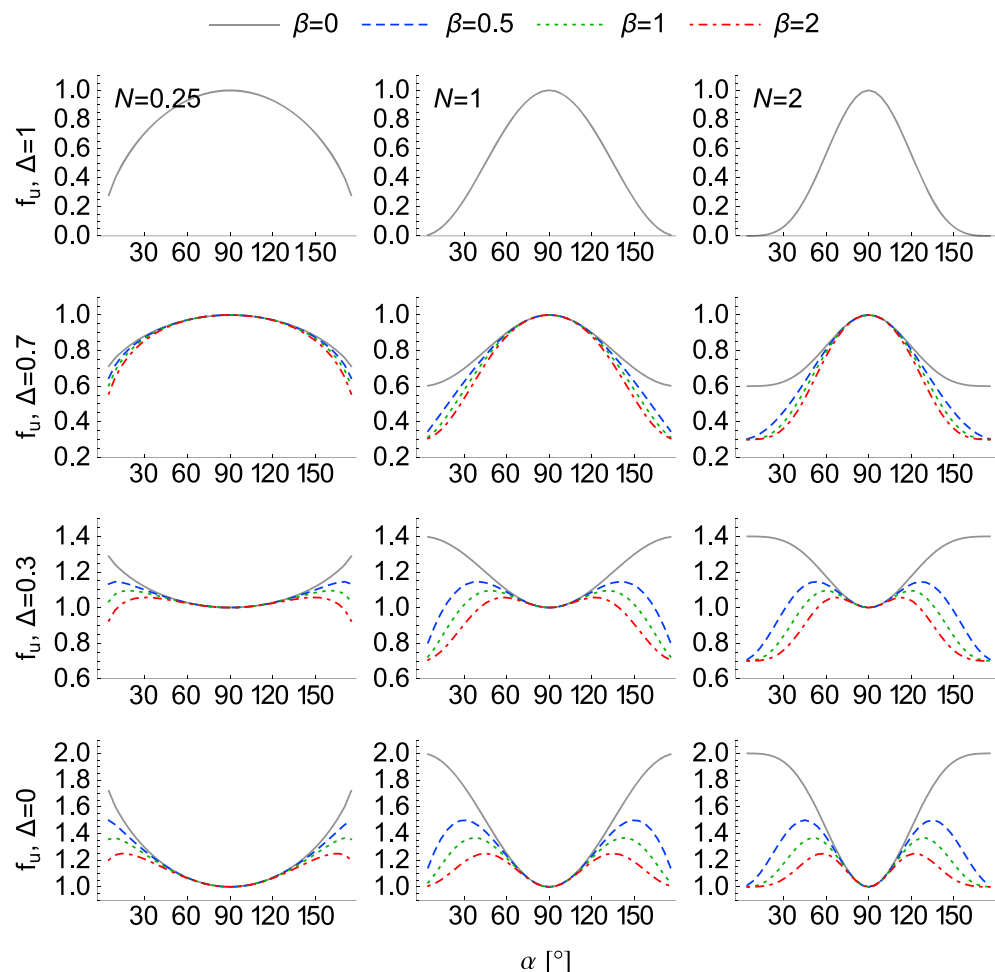
Figure 3. Pitch angle dependence of the base distribution function of equation (1) used to fit the observed ion fluxes. Four Δ values (1, 0.7, 0.3, and 0), three N values (0.25, 1, and 2), and four β values (0, 0.5, 1, and 2) are chosen for illustration.

The detailed fitting procedure is as follows. First, the 72 energy channels of the HOPE instrument are grouped into 18 (four channels per group). Individual groups represent individual components whose θ values are set to the mean value of the energies in the corresponding groups. Additionally, one more component is added to represent the thermal part whose temperature is set to 1 eV (the lowest energy measured is > 2 eV due to the spacecraft potential being $\approx$ 1.8 V). Second, the three free parameters in the $f_{u,s}$ term (N_s, Δ_s, and β_s) are adjusted to best represent the pitch angle dependence of the data in each group, where subscript s denotes a specific group. In this step, any data gaps that are present in He+ and O+ fluxes are interpolated from the general pitch angle dependence deduced from the known values as stated in the previous paragraph. Finally, while θ_s, N_s, Δ_s, and β_s are fixed, 19 multipliers (C_s) for the total distribution function $f_{\text{fit}} = \sum_{s=1}^{19} C_s \times f_{v,s} \times f_{u,s}$ are adjusted to globally minimize the difference between f_{fit} and f_{obs}.

The panels in the first row of Figure 4 display, from left to right, the fitting results of the observed fluxes of H+, He+, and O+ ion species, respectively. Compared to Figures 2b–2d, all the major features described in the beginning of this section are clearly visible in the fitted fluxes. The panels at the bottom row display relative differences between fitted and observed fluxes. At each energy channel, the median value of the relative difference across all pitch angle bins is chosen and displayed. So the fact that the relative differences are mostly less than 50% indicates that the fitted fluxes can accurately represent the data within a factor of 2 for most bins (for H+ ion fluxes almost all bins), although the maximum relative difference can be as large as an order of magnitude, especially at lower pitch angles. Table 1 lists in its 19 rows the fitting parameters
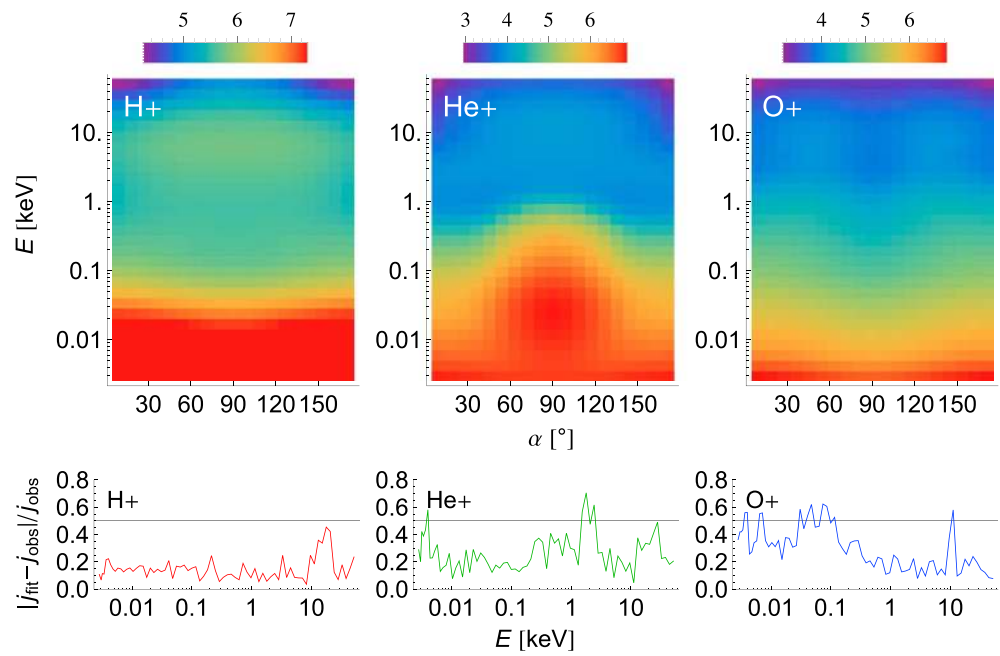
Figure 4. (top) Fitted ion distributions using multiples of equation (1), and (bottom) median values of relative errors of the fitting in each energy channel. Left, middle, and right columns correspond to H+, He+, and O+ ions, respectively.

corresponding to the 19 components for H+ ions (parameters for other species are available in the supporting information). The population numbers in the first column will be explained in section 4. Finally, the total plasma density estimated from the observed upper hybrid resonance line is $n_0 = 86.2$ cm^{-3}. The H+, He+, and O+ ions observed by HOPE constitute only 12.3%, 2%, and 1.4% of the total plasma ions,

Table 1. H+ Fitting Parameters

#[a]	η [b]	θ/v_A	n	Δ	β
First	0.0630854	0.0582954	0.577359	1.45648×10^{-6}	2.08525×10^{-6}
	0.0256976	0.102548	0.577359	1.45648×10^{-6}	2.08525×10^{-6}
	2.56676×10^{-8}	0.119505	9.99813	5.84504×10^{-6}	9.99771
Second	0.0116736	0.144623	0.768502	5.66574×10^{-6}	3.92054×10^{-6}
	0.0053029	0.182777	0.801365	6.54523×10^{-6}	1.60482×10^{-6}
	0.000559249	0.237274	0.747168	6.46534×10^{-8}	4.8132×10^{-9}
Third	0.00132532	0.313744	0.625936	2.84892×10^{-7}	5.60115×10^{-8}
	3.39471×10^{-6}	0.419897	0.329506	0.0000228989	0.0000283614
	0.000350528	0.565419	0.235843	6.59251×10^{-6}	0.0000113523
Fourth	0.000600232	0.764235	0.492135	0.011854	0.645039
	5.52695×10^{-7}	1.03509	0.555802	0.289829	0.709497
Fifth	0.00095827	1.40341	0.211425	0.584753	6.05657
	8.15537×10^{-7}	1.90395	1.63003	0.394284	0.703805
Sixth	5.34069×10^{-8}	2.58391	2.16001	0.298495	0.456934
	0.00195049	3.50733	1.02723	0.363128	0.675882
Seventh	0.00748442	4.76121	0.947356	0.414444	1.51689
	0.0000153403	6.46368	1.16232	0.659681	5.67479
Eighth	0.00352835	8.77518	1.67669	0.868871	4.19897
	0.000185188	11.9135	0.642699	0.921635	4.63192

[a]This column is referred to as "population number" in the text.
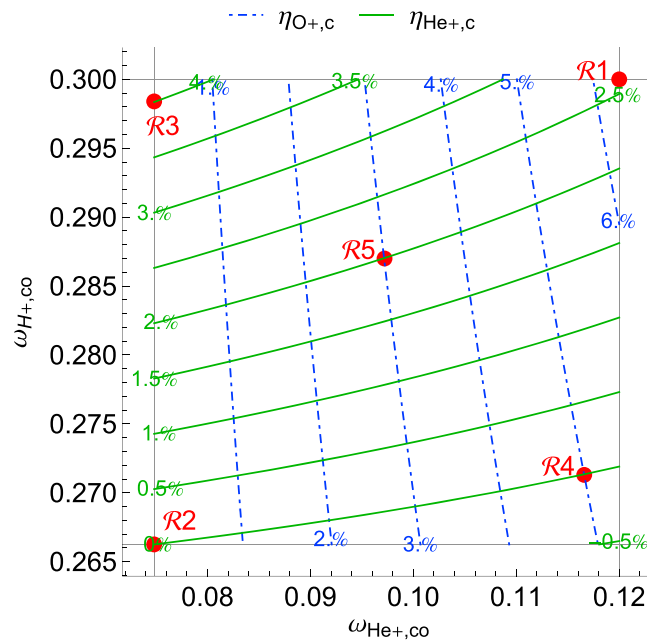[b]Concentrations are normalized to the total plasma density.

Figure 5. Dependence of $\eta_{O+,c}$ and $\eta_{He+,c}$ on $\omega_{He+,co}$ and $\omega_{H+,co}$ derived from the cold plasma dispersion relation. $\eta_{O+,c}$ and $\eta_{He+,c}$ values corresponding to the five filled circles are chosen for the linear analyses and hybrid simulations.

respectively. Thus, $\sim$84% of the ions are still missing from the measurement, which should be relatively cold ions below $\sim$2 eV of the spacecraft potential.

It is worth mentioning that potentially poor counting statistics of the measurements can introduce some uncertainties to the ion density estimates. We found that the relative errors of the density estimates can be 2%, 7%, and 28% for H+, He+, and O+ ions, respectively. However, some uncertainties in the observed warm H+, He+, and O+ concentrations will not significantly affect the following linear analyses and hybrid simulations. First, as will be described in section 4, the present study relies on the cutoff frequencies in the observed wave spectrum to infer the overall ion composition. Once the total H+, He+, and O+ concentrations have been determined, any errors in the observed warm ion concentra-

tions will be compensated by the corresponding cold ion concentrations. Second, the instability growth rate is mainly determined by the populations of energetic H+ ions, whose concentration has a small relative uncertainty, and is less sensitive to the exact shape of the distribution functions of He+ and O+ ions, whose concentrations have larger relative uncertainties. Therefore, the uncertainties in the observed ion concentrations have been neglected in the following analyses for simplicity.

4. Instability Analyses

The present study aims to examine the excitation of the observed EMIC waves using simultaneously measured ion distributions. However, due mainly to spacecraft surface charge, many of the cold ions $<\sim$2 eV are missing from the measurement. Although the density of the cold ions missed can be calculated using the plasma density estimated from the observed upper hybrid resonance line, the composition of these ions remains unknown and can significantly affect the excitation of EMIC waves. To overcome this difficulty, we here extract the cold ion concentrations based on the cutoff frequencies estimated from the observed wave spectrum. A similar method has been used previously by *Fraser et al.* [2005]. Hereafter, we will refer to the concentrations of cold H+, He+, and O+ ions as $\eta_{H+,c}$, $\eta_{He+,c}$, and $\eta_{O+,c}$, respectively, while the concentrations of the warmer ions measured by HOPE will be discriminated by replacing subscript c with w, denoting the warm components. Additionally, we will refer to the total (warm + cold) concentrations by omitting subscript c.

Characteristic frequencies in observed EMIC wave spectra have often been used to infer heavy ion concentrations [e.g., *Fraser et al.*, 2005; *Sakaguchi et al.*, 2013; *Matsuda et al.*, 2014]. The cold plasma dispersion relation in a multi-ion (H+, He+, and O+) plasma implies that quasi-parallel EMIC waves cannot propagate in two stop bands immediately above Ω_{He+} and Ω_{O+}. The upper bounds of the two stop bands are the H+ cutoff frequency ($\omega_{H+,co}$) and He+ cutoff frequency ($\omega_{He+,co}$), respectively. The values of the two cutoff frequencies are determined by the ion concentrations, η_{H+}, η_{He+}, and η_{O+} with $\eta_{H+} + \eta_{He+} + \eta_{O+} = 1$. On the other hand, if the two cutoff frequencies are known, e.g., estimated from observed wave spectra, the ion concentrations can then be inferred (see Appendix A). In Figure 2a, if we estimate $\omega_{He+,co} = 0.12\Omega_{H+}$ and $\omega_{H+,co} = 0.3\Omega_{H+}$ as suggested by the lower limits of the enhanced wave power spectrum in the He band and H band (denoted, respectively, by ω_1 and ω_2 in Figure 2a), we get $\eta_{H+} = 87.6\%$, $\eta_{He+} = 4.6\%$, and $\eta_{O+} = 7.8\%$. Since the warm ions observed by HOPE have already contributed $\eta_{H+,w} = 12.3\%$, $\eta_{He+,w} = 2.0\%$,

Table 2. Five Sets of Cold[a] Ion Concentrations Investigated

	$\eta_{H+,c}$	$\eta_{He+,c}$	$\eta_{O+,c}$
$\mathcal{R}1$	0.753	0.026	0.064
$\mathcal{R}2$	0.843	0	0
$\mathcal{R}3$	0.803	0.040	0
$\mathcal{R}4$	0.793	0	0.050
$\mathcal{R}5$	0.793	0.020	0.030

[a]Warm ion concentrations as observed are $\eta_{H+,w} = 0.123$, $\eta_{He+,w} = 0.020$, and $\eta_{O+,w} = 0.014$.

and $\eta_{O+,w} = 1.4\%$ as discussed in section 3, the cold ion concentrations are, therefore, inferred to be $\eta_{H+,c} = 75.3\%$, $\eta_{He+,c} = 2.6\%$, and $\eta_{O+,c} = 6.4\%$.

The estimates of $\omega_{He+,co} = 0.12\Omega_{H+}$ and $\omega_{H+,co} = 0.3\Omega_{H+}$ using the lower limits of the enhanced wave power spectrum in the He band and H band in Figure 2a are approximate, but the real values of $\omega_{He+,co}$ and $\omega_{H+,co}$ can only be smaller. Since η_{O+} monotonically decreases as either $\omega_{He+,co}$ or $\omega_{H+,co}$ decreases, the estimate of $\eta_{O+,c} = 6.4\%$ above is indeed the maximum possible $\eta_{O+,c}$. For η_{He+}, the situation is more complicated as it decreases with decreasing $\omega_{H+,co}$ but increases with decreasing $\omega_{He+,co}$ as discussed in Appendix A. To examine the possible variation of $\eta_{O+,c}$ and, especially, $\eta_{He+,c}$ due to uncertainty in the estimates of $\omega_{He+,co}$ and $\omega_{H+,co}$, Figure 5 shows a map of $\eta_{O+,c}$ and $\eta_{He+,c}$ as functions of $\omega_{He+,co}$ and $\omega_{H+,co}$ across ranges of possible values of $\omega_{He+,co}$ and $\omega_{H+,co}$ from the observed wave spectrum. This figure illustrates the analysis in Appendix A: η_{He+} strongly influences $\omega_{H+,co}$ but not $\omega_{He+,co}$, whereas η_{O+} influences both cutoff frequencies ($\omega_{He+,co}$ more strongly than $\omega_{H+,co}$). The values of $\eta_{He+,c} = 2.6\%$ and $\eta_{O+,c} = 6.4\%$ (inferred from $\omega_{He+,co} = 0.12\Omega_{H+}$ and $\omega_{H+,co} = 0.3\Omega_{H+}$) are denoted by $\mathcal{R}1$ at the upper right corner. In contrast, $\mathcal{R}2$ at the lower left corner represents the extreme situation when all the cold ions not measured by HOPE are H+ so that $\eta_{He+,c} = 0\%$ and $\eta_{O+,c} = 0\%$. Furthermore, we labeled three additional points in the map: $\mathcal{R}3$ denotes the situation when $\omega_{He+,co}$ is at its minimum and $\omega_{H+,co}$ is close to its maximum, which lead to large $\eta_{He+,c} = 4.0\%$ while $\eta_{O+,c} = 0\%$; $\mathcal{R}4$ represents the situation when $\omega_{H+,co}$ is near its minimum and $\omega_{He+,co}$ is close to its maximum, which corresponds to $\eta_{He+,c} = 0\%$ while $\eta_{O+,c} = 5.0\%$; $\mathcal{R}5$ represents an intermediate situation when $\omega_{H+,co}$ and $\omega_{He+,co}$ both have intermediate values which lead to $\eta_{He+,c} = 2.0\%$ and $\eta_{O+,c} = 3.0\%$. Finally, Table 2 summarizes the cold ion concentrations corresponding to these five situations.

With the warm ion distributions directly measured and the cold ion concentrations inferred, we perform linear instability analysis following the method described by *Chen et al.* [2013, equations (14) through (17)]. We solve $D_r(\omega, k_\parallel) = 0$ [*Chen et al.*, 2013, equation (8)] for the real part of the frequency, ω, for given parallel wave numbers, $k_\parallel$. With the ω-$k_\parallel$ relation determined, we then calculate growth rate, γ, using equation (9) of [*Chen et al.*, 2013]. Here we have limited our interest to EMIC waves propagating parallel to the background magnetic field because linear theory reveals maximum growth rate at parallel propagation, and the observation shows that the wave normal angles are small ($\sim 20°$; Figure 1c). In addition, since the instability analysis formulation

Table 3. Parameters of Eight Bi-Maxwellian[a] Populations

	η	$\theta_\parallel / v_A$	$\theta_\perp / v_A$	
First	0.088783	0.0799632	0.0706452	
Second	0.0175358	0.175225	0.152908	
Third	0.00167924	0.407021	0.36652	
Fourth	0.000600785	0.805293	0.743307	
Fifth	0.000959085	1.36681	1.42209	H+
Sixth	0.00195054	3.46478	3.52838	
Seventh	0.00749976	4.57512	4.85762	
Eighth	0.00371354	6.94102	9.81191	
First	0.00535818	0.0471593	0.0408901	
Second	0.00362649	0.0920812	0.12989	
Third	0.00986801	0.137099	0.243598	
Fourth	0.000698919	0.236997	0.462697	
Fifth	1.85066×10^{-20}	0.839738	1.00339	He+
Sixth	0.000100781	1.39448	1.23753	
Seventh	0.00040093	2.77078	3.28961	
Eighth	0.000203992	4.93851	5.95312	
First	0.0109041	0.0197329	0.0171176	
Second	0.000978582	0.0626641	0.0541212	
Third	0.000561219	0.139481	0.1205	
Fourth	0.000282203	0.284042	0.24509	
Fifth	0.000363228	0.406149	0.374822	O+
Sixth	0.0000522083	0.672612	0.637007	
Seventh	0.000847438	1.46365	1.37739	
Eighth	0.000298454	2.7077	3.10466	

[a]$f_{bi} = \exp(-v_\parallel^2/\theta_\parallel^2 - v_\perp^2/\theta_\perp^2)/(\pi^{3/2}\theta_\parallel\theta_\perp^2)$ where $\theta_{(\parallel,\perp)} = \sqrt{2T_{(\parallel,\perp)}/m}$.
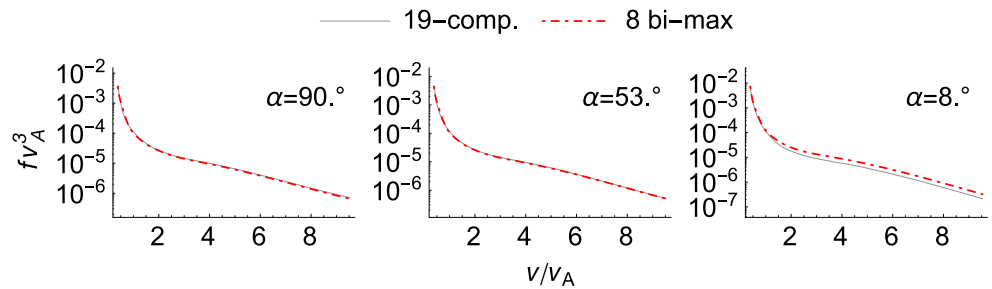
Figure 6. Comparison between the 19-component fitted distribution in section 3 and the simplified eight bi-Maxwellian velocity distribution in section 4 for H+ at three selected pitch angles.

used is based upon bi-Maxwellian distributions, we further reduce, for each ion species, the observed warm ions into eight bi-Maxwellian ion populations from the fitted 19 components in section 3. For example, first of the eight bi-Maxwellian H+ populations is derived from the three fitted H+ components denoted by population number "First" in the first column of Table 1. The density of the new bi-Maxwellian H+ popula-tion is the total density of the three fitted components. The parallel and perpendicular temperatures of the new population, similarly, are the density-weighted average of the corresponding temperatures of the three fitted components. Table 3 lists the derived bi-Maxwellian parameters for all three ion species. Figure 6
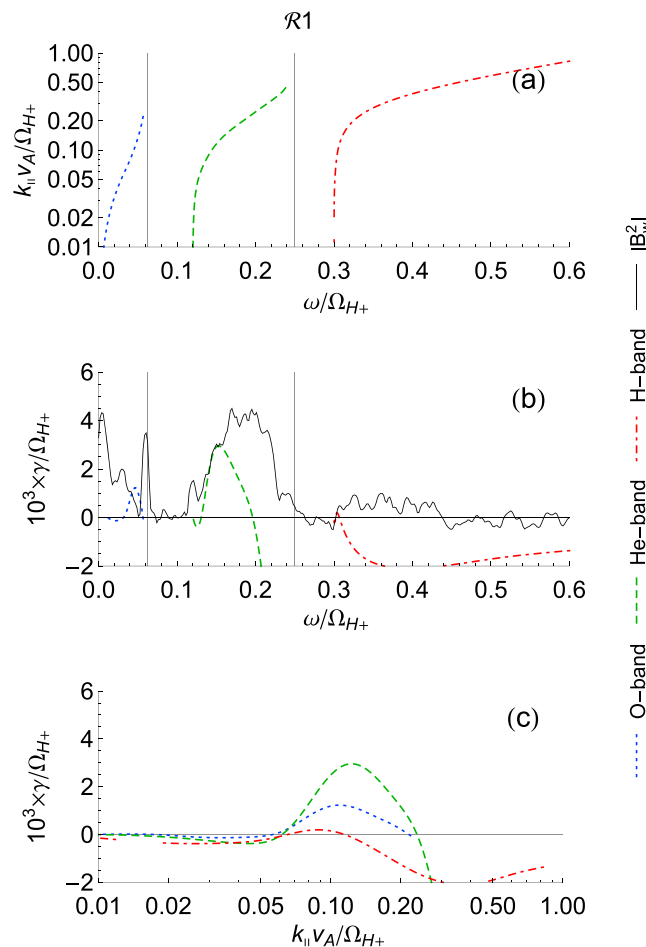

Figure 7. EMIC wave dispersion relation and wave growth rate for $\mathcal{R}1$. (a) Parallel wave number and (b) growth rates as a function of the fre-quency, and (c) growth rates as a function of the parallel wave number. The solid curve in Figure 7b represents the observed wave spectrum (scaled).

shows comparison between the eight bi-Maxwellian H+ distribution calcu-lated using the parameters listed in Table 3 and the 19-component fitted H+ distribution in section 3 at three different pitch angles (90°, 53°, and 8°). The two distributions agree with each other extremely well except for very small pitch angles (Figure 6 (right) with $\alpha = 8°$). Nevertheless, the effect of non-bi-Maxwellian features related to the deviation will be discussed in section 6.

Using parameters listed in Table 3 for the warm ions captured by HOPE, instability analysis has first been carried out for $\eta_{He+,c} = 2.6\%$ and $\eta_{O+,c} = 6.3\%$, the first situation ($\mathcal{R}1$) of the cold ion concentrations sum-marized in Table 2. Figure 7 displays the results. Two stop bands clearly emerge as seen in Figure 7a. Figure 7b shows that the strongest instability occurs in the He band with maximum growth rate of $\gamma/\Omega_{H+} \approx 3 \times 10^{-3}$. For comparison, the observed wave spectrum (after being accordingly scaled) is included in Figure 7b as the solid curve. There exists substantial positive growth rate in the O band close to Ω_{O+}, whereas damping occurs in the H band except for the very narrow frequency range imme-diately above $\omega_{H+,co}$; these are more

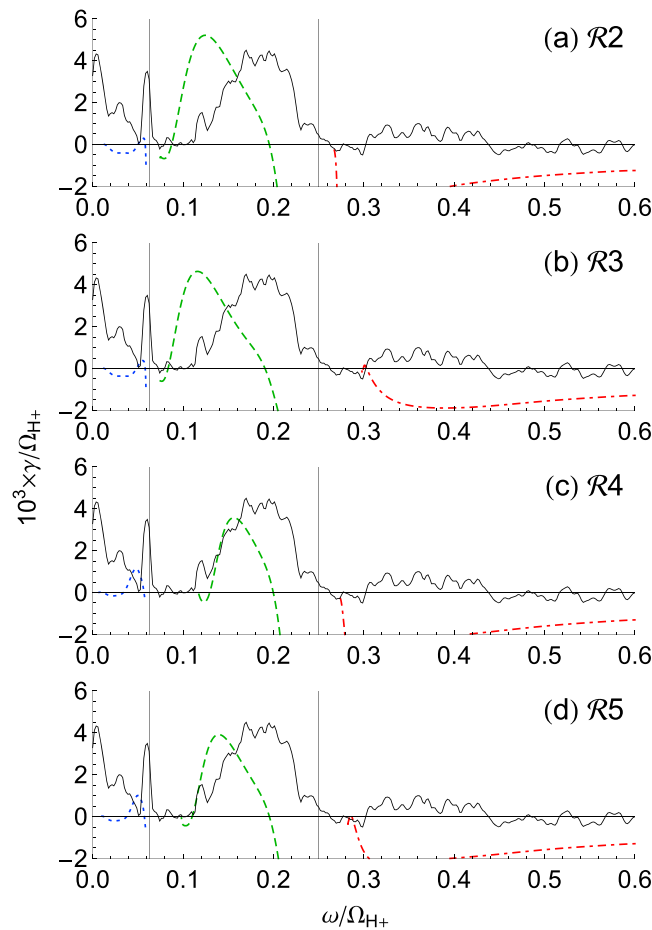**Figure 8.** (a–d) Growth rates as a function of the frequency for $\mathcal{R}2$–$\mathcal{R}5$ cases, respectively. The figure format is the same as that of Figure 7b.

clearly seen in Figure 7c. The peak frequency of the He band growth rate, which is at $\sim 0.16\Omega_{H+}$, is slightly smaller than the peak frequency of the observed wave spectrum at $\sim 0.18\Omega_{H+}$ (solid curve).

Related to the uncertainties in the inferred cold ion concentrations, instability analysis has also been performed for the other four situations ($\mathcal{R}2$–$\mathcal{R}5$) summarized in Table 2 to investigate how the instability growth rate varies with possible changes in the cold ion composition. Figure 8 presents growth rate as a function of ω/Ω_{H+} for these four situations. First, the largest instability occurs consistently in the He band for all situations, but the maximum growth rate is greatly affected by $\eta_{O+,c}$ and, to a lesser extent, by $\eta_{He+,c}$; it can be as large as $\gamma/\Omega_{H+} \approx 5\times10^{-3}$ for $\mathcal{R}2$ (Figure 8a). Second, with an increase of $\eta_{O+,c}$, the peak frequency of He band instability moves toward larger frequency, up to $\sim 0.16\Omega_{H+}$ (yet still smaller than that of observed spectrum), and so does $\omega_{He+,co}$. Finally, with increasing $\eta_{He+,c}$, very weak and narrow frequency band instability in the H band starts to develop right above $\omega_{H+,co}$ (Figures 7 and 8b) that may correspond to the
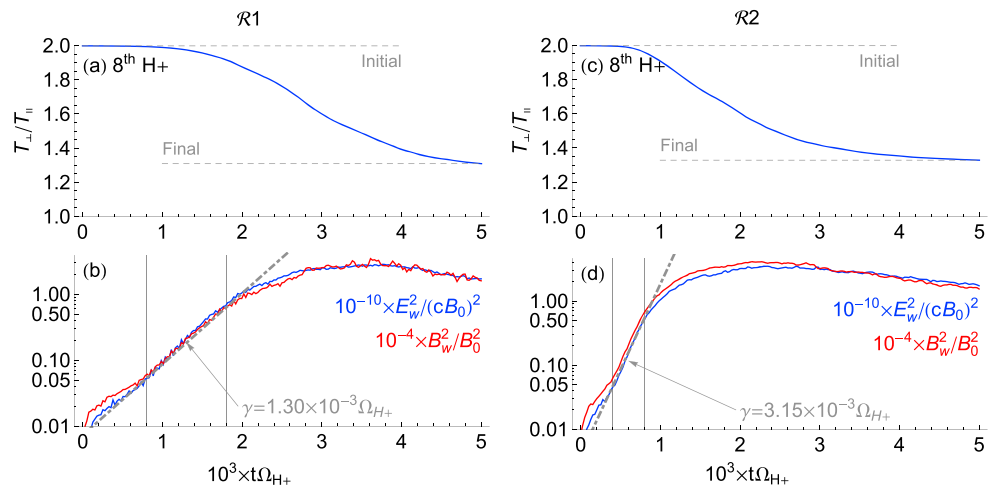
lower frequency end of the observed weak H band waves. Likewise, with increasing $\eta_{O+,c}$, instability in the O band is substantially enhanced right below Ω_{O+}, which, however, is not seen from the observation.

5. Hybrid Simulations

Besides the linear analyses as described in section 4, one-dimensional, self-consistent hybrid simulations are carried out to simulate the enhanced waves observed. We adopt the same hybrid code used in *Liu et al.* [2010], which treats plasma ions as superparticles but electrons as a massless, charge-neutralizing, adiabatic fluid [*Winske and Omidi*, 1993]. Five simulation runs are performed corresponding to the five situations of the cold ion concentrations $\mathcal{R}1$–$\mathcal{R}5$ in Table 2. In each run, the periodic simulation domain is in the direction of the background magnetic field and its size is $L_x = 1000\lambda_{H+}$, where $\lambda_{H+} = \sqrt{m_{H+}/n_0\mu_0 e^2}$ is the ion inertial length. There are $N_x = 512$ grids so that all the unstable modes predicted by the linear analyses are well resolved. The simulation time step is $0.05\Omega_{H+}$. All runs are initialized with the identical warm ion parameters listed in Table 3 and with $\omega_{pe}/\Omega_{ce} = 29.5$ (corresponding to $c/v_A = 1.26 \times 10^3$, where c and v_A are the speed of light and Alfvén speed, respectively). The only difference comes from the cold ion composition shown in Table 2. Needed by the simulation code, the temperatures of the cold ions, which are isotropic, are set to 1% of the parallel temperature of the first bi-Maxwellian population of the corresponding ion species in Table 3. Given the low amplitude of the enhanced waves expected, 10^4 superparticles per cell have been used to represent each population, including both the cold ion population and the eight warm bi-Maxwellian populations, of every ion species.

Figure 9 shows time evolution of (top) $T_{\perp,8^{th}H+}/T_{\parallel,8^{th}H+}$ (temperature anisotropy of the eighth H+ population in Table 3, which is the major population driving the instability) and (bottom) the electric and magnetic

Figure 9. Time evolution of the simulated system for (a–b) $\mathcal{R}1$ and (c–d) $\mathcal{R}2$ cases. The first row shows the temperature anisotropy of the eighth H+ component, and the second row shows the electric and magnetic field energy. The dash-dotted lines are fit to $\sim \exp(2\gamma t)$ between the time interval indicated by the two vertical lines.
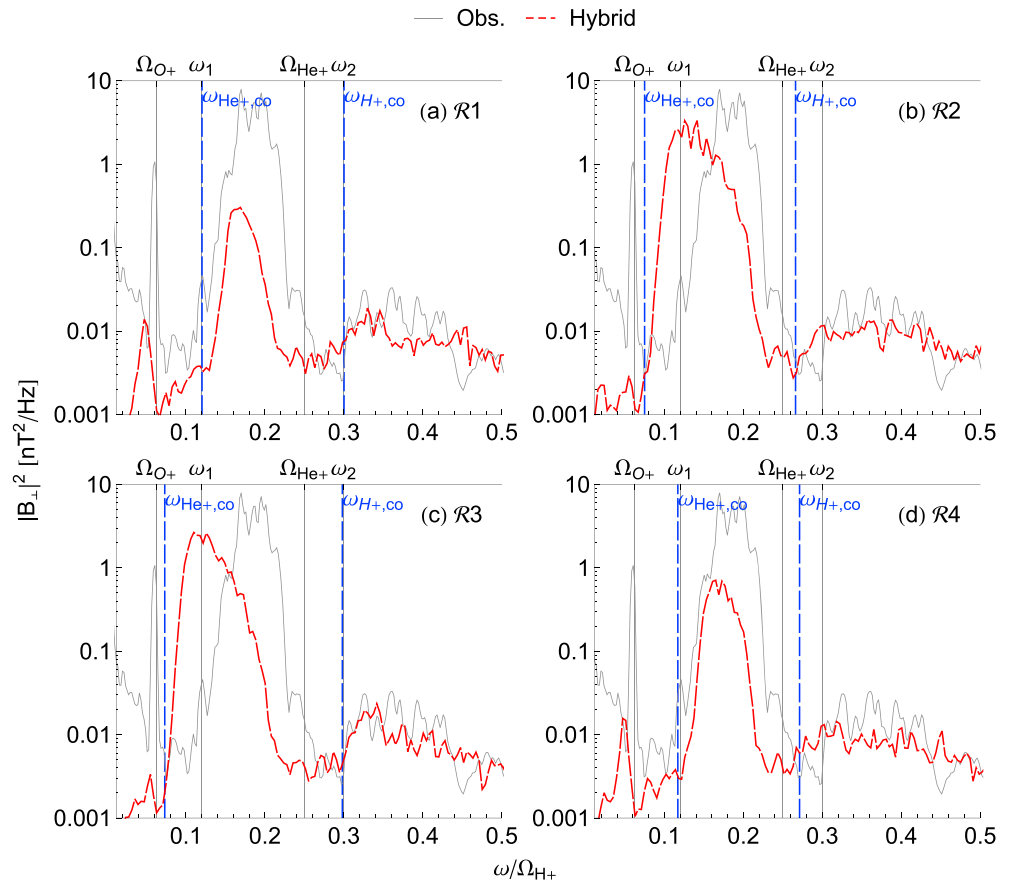

Figure 10. (a–d) Comparison of the simulated wave power spectra (broken curves) for $\mathcal{R}1$–$\mathcal{R}4$ cases, respectively, with the observed wave spectrum (solid curves). The two vertical gray lines denoted by ω_1 and ω_2 are the lower frequency limits of the wave spectral peaks in the He band and H band shown in Figure 2. $\omega_{He+,co}$ and $\omega_{H+,co}$ marked by the two vertical blue dashed lines are the cutoff frequencies obtained from Figure 5.
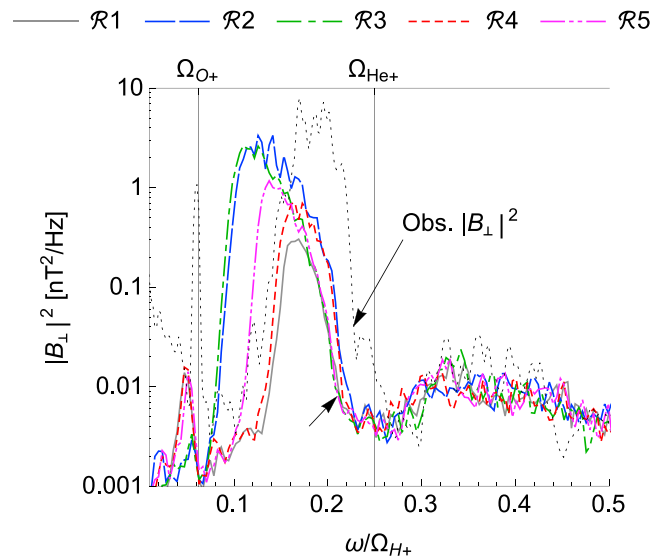
Figure 11. The simulated wave spectra of all five simulations plotted on the same panel for comparison. The dotted curve represents the observed spectrum. The two arrows denote the trailing edge of the He band waves.

field energies for $\mathcal{R}1$ and $\mathcal{R}2$, respectively. Clearly, the electromagnetic waves develop at the expense of free energy stored in the energetic anisotropic protons whose anisotropy decreased from initially 2 to 1.3 at the end of the run. In contrast, temperature anisotropies of other populations either stayed the same or increased slightly (not shown). The exponential growth phases (energy $\sim \exp(2\gamma t)$) occur between $t \sim 800/\Omega_{H_+}$ and $t \sim 2000/\Omega_{H_+}$ for $\mathcal{R}1$ and between $t \sim 400/\Omega_{H_+}$ and $t \sim 800/\Omega_{H_+}$ for $\mathcal{R}2$, indicated by two vertical lines. As shown in the instability analysis, the waves for $\mathcal{R}2$ grow faster than the waves for $\mathcal{R}1$. By assessing the slopes between these two dashed lines, the estimated growth rates for $\mathcal{R}1$ and $\mathcal{R}2$ are $\sim 1.30 \times 10^{-3}\Omega_{H_+}$ and $\sim 3.15 \times 10^{-3}\Omega_{H_+}$, respectively, which are about half the maximum

growth rates calculated from the linear analyses in section 4. This is not surprising because the maximum growth rate from linear theory addresses only the single mode of maximum growth, whereas the estimated growth rates from the simulations average over all the growing modes. The saturation level of the magnetic field energy for both runs is roughly $2 \times 10^{-4}B_0^2$ which is close to the observed one of $1.06 \times 10^{-4}B_0^2$, where $B_0 \approx 101$ nT is the background magnetic field. Apart from the saturation levels and growth rates, the general pictures of time evolution of all other runs are consistent (not shown).

Figure 10 displays magnetic field wave spectra perpendicular to the background magnetic field as a function of frequency for $\mathcal{R}1$–$\mathcal{R}4$. The simulated fluctuations are taken between $200/\Omega_{H_+}$ and $1800/\Omega_{H_+}$, representing the exponential growth phase, to perform the Fourier analysis. For the case with the fastest growing waves, $\mathcal{R}2$, this interval may be too long, but after some experiments, the results for the maximum time limit less than $1800/\Omega_{H_+}$ were generally consistent. We choose a long duration to achieve high-frequency resolutions in the calculated wave spectra. The general picture is remarkably consistent with the growth rates calculated from linear theory shown in Figures 7b and 8a–8c. Namely, the He band waves develop fastest and strongest; the peak wave amplitudes and the frequencies at those peaks for the He band are strongly dependent upon the heavy ion concentrations; the O band wave power, the minor local maximum right below Ω_{O_+}, strongly depends upon $\eta_{O_+,c}$ but is less sensitive to $\eta_{He_+,c}$; and the waves are suppressed in the two stop bands whose widths vary with the cold ion concentrations.

For comparison, the observed wave spectrum is plotted as the light curves in Figure 10. Note that the real units (nT^2/Hz) are used for direct comparison. ω_1 and ω_2 denote the same frequencies as those in Figure 2a, and the long-dashed vertical lines labeled by $\omega_{He_+,co}$ and $\omega_{H_+,co}$ are the corresponding cutoff frequencies from Figure 5. In all cases, the He band waves develop right above $\omega_{He_+,co}$. As a result, $\mathcal{R}1$ and $\mathcal{R}4$, where $\eta_{He_+,c}$ and $\eta_{O_+,c}$ are set such that $\omega_{He_+,co} = \omega_1$, better represent the leading slope of the observed He band spectrum. Such distinction for the H band is not so clear due to very weak, if any, wave power. Therefore, comparison of the stop band above Ω_{He_+} is not appropriate. Nevertheless, for all cases, the waves are slightly suppressed in the frequency range below $\omega_{H_+,co}$ indicating presence of the stop band above Ω_{He_+}.

Figure 11, displaying spectra of all five runs, further elucidates the pivotal role of the heavy ion concentrations in controlling the He band wave spectrum and the width of the stop band above Ω_{O_+}. Not surprisingly, the spectrum of $\mathcal{R}5$ lie in the middle of the other runs. Consistent with the linear analyses in section 4, the spectrum of the excited waves is more sensitive to $\eta_{O_+,c}$ than $\eta_{He_+,c}$. Increasing $\eta_{O_+,c}$ weakens the He band waves but enhances the O band waves. In addition, the cutoff frequency $\omega_{He_+,co}$ revealed by the simulated wave spectra agrees with the expectation from the instability analyses. Finally, the results of Figures 10 and

11 suggest that the frequency range of the excited He band waves and the width/location of the stop band immediately above Ω_{O+} in $\mathcal{R}1$ and $\mathcal{R}4$ best match those of the observation. Therefore, according to Figure 5 and Table 2, the real $\eta_{O+,c}$ is likely between 5% and 6.4% and $\eta_{He+,c}$ between 0% and 2.6%. The uncertainty of $\eta_{He+,c}$ is larger because the He+ concentration mainly controls the width of the stop band above Ω_{He+} which cannot be accurately determined in $\mathcal{R}1$ and $\mathcal{R}4$ due to the weak, if any, H band waves simulated.

6. Discussions

Figure 11 reveals one interesting feature of the simulated spectra that the upper frequency bound of the He band waves excited, i.e., the highest frequency in the He band peak above the noise floor, is insensitive to the changes of the cold ion concentrations. This feature is consistent with the results of the instability analyses shown in Figure 8. However, the locations of this upper bound in the simulated spectra are below the observed one. Additionally, even for the simulated wave spectra in $\mathcal{R}1$ and $\mathcal{R}4$, for which the frequency range of the excited He band waves best matches the observed waves, the He band peak frequencies are clearly lower than the observed value. These discrepancies are, at least partially, related to the fact that our instability analyses and hybrid simulations have used the observed ion distributions which likely correspond to the stage when the waves have already developed and the original, supposedly more anisotropic, ion distributions have already yielded a substantial amount of their free energy to the wave excitation. As shown by previous hybrid simulations, e.g., Figure 1 in *Liu et al.* [2010], when an initially anisotropic ion distribution excites EMIC waves through the ion cyclotron instability, the enhanced waves, in turn, scatter the anisotropic ions and reduce their anisotropy until the system reaches the quasi-steady phase when the plasma becomes "marginally" stable. Ideally, one should choose the initial ion parameters in a hybrid simulation so that, in the quasi-steady phase, the scattered ions have distributions as observed. The corresponding waves should then better match the observed ones. In fact, according to our linear instability analyses, one effective way to increase the upper frequency bound and the peak growth rate frequency of the unstable He band waves is by modifying the warm ion populations, especially the three warmest H+ populations (the sixth–eighth populations of H+ ions) and the three coolest He+ populations (the first–third populations of He+ ions) in Table 3. Increasing anisotropies of these three energetic H+ populations raises the overall growth rate. Decreasing the thermal temperatures of the three cool He+ populations decreases the damping at large wave number. Combined together, these modifications can raise the upper frequency bound and the peak growth rate frequency of the unstable He band waves toward the observed ones. Accordingly, we have carried out several hybrid simulations using increased H+ anisotropies hoping that the scattered H+ in the quasi-steady phase would have "residual" anisotropies closer to the observed ones. However, the H+ anisotropies in the quasi-steady phase of these runs turned out to be even smaller than before. This seemingly unexpected result is indeed not surprising: Larger initial H+ anisotropies lead to stronger waves in the system, which scatter the ions more significantly, leading to smaller H+ anisotropies in the quasi-steady phase. Similar results for whistler waves excited through the whistler anisotropy instability driven by anisotropic electrons have been reported by *Fu et al.* [2014].

The hybrid simulations in the present study have simulated the wave excitation as an initial value problem in an isolated system and used periodic boundary conditions for simplicity. In reality, the system may have very dynamic free energy input through energetic anisotropic ion injections. Moreover, unlike in our simulations, the excited waves can propagate away from the excitation region, so the wave amplitude in the source region should be smaller. This implies less scattering of the anisotropic ions and larger residual anisotropies in the quasi-steady phase. To overcome these limitations as well as the dilemma discussed in the previous paragraph, in the present work, we have chosen to focus on the linear growth phase of the simulations instead of the more commonly used quasi-steady phase. Compared to the quasi-steady phase, the amplitude of the enhanced waves is smaller, but the ion distributions are closer to the observed ones during the linear growth phase. Although not investigated in this study, a driven simulation in which a fraction of the energetic H+ populations are refreshed regularly to keep the anisotropies large (effectively representing the energetic anisotropic ion injections) [*Denton et al.*, 1993] may be another way to overcome the limitations.

In the observed wave spectrum shown in Figure 2a, other than the nonphysical peak at Ω_{O+}, there is no significant wave enhancement below Ω_{O+}. On the other hand, the simulated wave spectra in the $\mathcal{R}1$ and $\mathcal{R}4$ cases, for which the frequency range of the excited He band waves best matches the observed waves
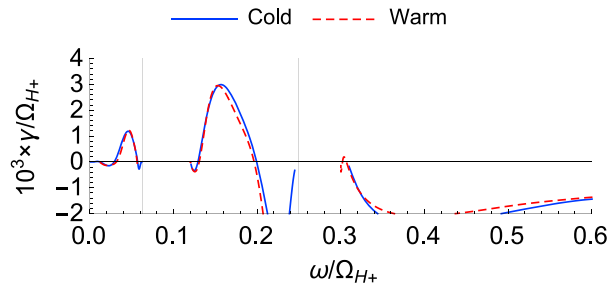
Figure 12. Comparison of growth rate calculated using the 19-component fitted ion distributions with the growth rate calculated using the eight bi-Maxwellian distributions (see section 6).

among the five simulation cases presented, demonstrate enhanced O band waves. We have no firm explanation for this discrepancy, but one possible reason is that the O band peak in the simulated wave spectra may be below the noise level of the observed spectrum (Figure 11; note that we are using the same units). Thus, there may be wave growth in the O band which is just buried by the noise floor in the observed spectrum. In addition, our linear instability analyses suggest insignificant H band wave growth, opposed to the observed spectrum which displays some H band waves. Although the simulated spectra (in all five cases) seem to demonstrate a weak peak in H band, the "standing-out" of the peak is mainly due to the more severely attenuated fluctuations in the stop band above Ω_{He+} and the H band peak is too weak to be reliably identified as enhanced EMIC waves. However, as discussed above, the observed ion distributions, which have been used for our instability analyses and hybrid simulations, likely correspond to the stage when the waves have already developed. The observed H band waves may have been driven by the original, supposedly more anisotropic, ion distributions.

Finally, we examine the possible consequences of reducing the 19-component fitted distributions of the observed warm ions to the eight bi-Maxwellian populations on the instability analyses in section 4. To check whether any non-bi-Maxwellian features not captured by the eight bi-Maxwellian distributions significantly change the analysis results, we additionally performed the growth rate calculation using the cold plasma dispersion relation (equation (19) instead of equation (14) in *Chen et al.* [2013]) directly for the 19-component fitted distributions of all ion species obtained in section 3, with the cold ion concentrations of $\mathcal{R}1$. Use of the cold plasma dispersion relation is to avoid two-dimensional numerical integration involved with the real part of the dispersion relation for the velocity distribution function of equation (1), but we confirmed that the warm plasma effect on the real part of the dispersion relation is negligible. Figure 12 compares the result to the growth rate calculation shown in Figure 7b, which is for the eight bi-Maxwellian distributions. There are some minor differences, such as in the trailing slope of the He band growth rate, but the overall deviation is small. Thus, our instability analyses based on the eight bi-Maxwellian populations in section 4 are generally reliable.

7. Summary

We have performed an event study to investigate EMIC wave excitation using the simultaneously measured ion distributions with Van Allen Probes data. We were able to extract the distributions of warm heavy ions as well as anisotropic energetic protons that drive the wave growth. Cold ions below ~2 eV not captured by HOPE have been inferred using the cutoff frequencies estimated from the observed wave spectrum. Hybrid simulations coupled with the instability analyses demonstrated that these distributions can spontaneously and self-consistently excite EMIC waves in the frequency range consistent with that of the observed wave spectrum. By varying the inferred cold ion concentrations in a reasonable range, the simulated waves generally vary as predicted by linear theory. It is found that the excited waves are more sensitive to the cold O+ concentration than the cold He+ concentration. Increasing the cold O+ concentration weakens the He band waves but enhances the O band waves.

Appendix A: Estimate Ion Concentrations From Cutoff Frequencies

We start from the cold plasma dispersion relation for parallel propagating EMIC waves in a multi-ion (H+, He+, and O+) plasma [*Summers and Thorne*, 2003, equation (2)]:

$$\left(\frac{kc}{\omega}\right)^2 = 1 - \frac{\omega_{pe}^2}{\Omega_{ce}^2 \epsilon x}\left(\frac{1}{1+\epsilon x} + \frac{\eta_{H+}}{x-1} + \frac{\eta_{He+}}{4x-1} + \frac{\eta_{O+}}{16x-1}\right), \tag{A1}$$

where $\epsilon \approx 1/1836$ is electron to proton mass ratio, k is the wave number, c is the speed of light, and $x = \omega/\Omega_{H+}$. Utilizing the fact that $k \to 0$ at cutoff frequencies, $\epsilon \ll x < 1$, and $\Omega_{ce}^2/\omega_{pe}^2 \leq \sim 1$ (for our event), one can reduce equation (A1) to

$$0 \approx 1 + \frac{\eta_{H+}}{x-1} + \frac{\eta_{He+}}{4x-1} + \frac{\eta_{O+}}{16x-1}. \tag{A2}$$

Since the $x = 0$ root is obvious, one can, after using $\eta_{H+} + \eta_{He+} + \eta_{O+} = 1$, finally get a quadratic equation of x as follows

$$0 = 64x^2 - 4(12\eta_{He+} + 15\eta_{O+} + 5)x + 3(\eta_{He+} + 5\eta_{O+}) + 1. \tag{A3}$$

Solving for x, two cutoff frequencies for the given heavy ion concentrations can be found

$$\left\{ \begin{matrix} \omega_{H+,co} \\ \omega_{He+,co} \end{matrix} \right\} = \left(5 + 12\eta_{He+} + 15\eta_{O+} \pm 3\sqrt{16\eta_{He+}^2 + (1-5\eta_{O+})^2 + 8\eta_{He+}(1+5\eta_{O+})} \right) \times \frac{\Omega_{H+}}{32}. \tag{A4}$$

For the limiting case of $\eta_{O+} \to 0$, equation (A4) can be simplified to

$$\frac{\omega_{H+,co}}{\Omega_{H+}} = \frac{1+3\eta_{He+}}{4}, \text{ and } \frac{\omega_{He+,co}}{\Omega_{H+}} = \frac{1}{16}, \tag{A5}$$

the former of which is equivalent to equation (2) of *Gary et al.* [2012].

On the other hand, if the two cutoff frequencies are known (for example, estimated from observed wave spectrum), one may deduce the ion concentrations using equation (A3). For this purpose, it is convenient to rewrite equation (A3) as

$$0 = 3(1-16x)\eta_{He+} + 15(1-4x)\eta_{O+} + (1-4x)(1-16x). \tag{A6}$$

Substituting the two known cutoff frequencies into equation (A6) leads to two simultaneous linear equations, which can be solved for η_{He+} and η_{O+}. After some algebra, the results are

$$\eta_{He+} = \frac{4}{9}\left(4\frac{\omega_{H+,co}}{\Omega_{H+}} - 1\right)\left(1 - 4\frac{\omega_{He+,co}}{\Omega_{H+}}\right), \text{ and } \eta_{O+} = \frac{1}{45}\left(16\frac{\omega_{H+,co}}{\Omega_{H+}} - 1\right)\left(16\frac{\omega_{He+,co}}{\Omega_{H+}} - 1\right). \tag{A7}$$

Equation (A7) has been used in the present study to calculate heavy ion concentrations from cutoff frequencies estimated from the observed EMIC wave spectrum. In addition, since $\frac{\omega_{H+,co}}{\Omega_{H+}} > \frac{1}{4}$ and $\frac{1}{4} > \frac{\omega_{He+,co}}{\Omega_{H+}} > \frac{1}{16}$, it can be readily seen that η_{He+} increases with increasing $\omega_{H+,co}/\Omega_{H+}$ but decreases with increasing $\omega_{He+,co}/\Omega_{H+}$. On the other hand, η_{O+} monotonically increases as either $\omega_{H+,co}/\Omega_{H+}$ or $\omega_{He+,co}/\Omega_{H+}$ increases.

References

Anderson, B. J., and S. A. Fuselier (1994), Response of thermal ions to electromagnetic ion cyclotron waves, *J. Geophys. Res.*, *99*(A10), 19,413–19,425, doi:10.1029/94JA01235.

Ashour-Abdalla, M., and C. F. Kennel (1978), Nonconvective and convective electron cyclotron harmonic instabilities, *J. Geophys. Res.*, *83*(A4), 1531–1543, doi:10.1029/JA083iA04p01531.

Blum, L. W., E. A. MacDonald, S. P. Gary, M. F. Thomsen, and H. E. Spence (2009), Ion observations from geosynchronous orbit as a proxy for ion cyclotron wave growth during storm times, *J. Geophys. Res.*, *114*, A10214, doi:10.1029/2009JA014396.

Blum, L. W., E. A. MacDonald, L. B. N. Clausen, and X. Li (2012), A comparison of magnetic field measurements and a plasma-based proxy to infer EMIC wave distributions at geosynchronous orbit, *J. Geophys. Res.*, *117*, A05220, doi:10.1029/2011JA017474.

Bortnik, J., R. M. Thorne, T. P. O'Brien, J. C. Green, R. J. Strangeway, Y. Y. Shprits, and D. N. Baker (2006), Observation of two distinct, rapid loss mechanisms during the 20 November 2003 radiation belt dropout event, *J. Geophys. Res.*, *111*, A12216, doi:10.1029/2006JA011802.

Chen, L., R. M. Thorne, and R. B. Horne (2009), Simulation of EMIC wave excitation in a model magnetosphere including structured high-density plumes, *J. Geophys. Res.*, *114*, A07221, doi:10.1029/2009JA014204.

Chen, L., R. M. Thorne, V. K. Jordanova, C.-P. Wang, M. Gkioulidou, L. Lyons, and R. B. Horne (2010), Global simulation of EMIC wave excitation during the 21 April 2001 storm from coupled RCM-RAM-HOTRAY modeling, *J. Geophys. Res.*, *115*, A07209, doi:10.1029/2009JA015075.

Chen, L., R. M. Thorne, and J. Bortnik (2011), The controlling effect of ion temperature on EMIC wave excitation and scattering, *Geophys. Res. Lett.*, *38*, L16109, doi:10.1029/2011GL048653.

Chen, L., R. M. Thorne, Y. Shprits, and B. Ni (2013), An improved dispersion relation for parallel propagating electromagnetic waves in warm plasmas: Application to electron scattering, *J. Geophys. Res. Space Physics*, *118*, 2185–2195, doi:10.1002/jgra.50260.

Chen, L., V. K. Jordanova, M. Spasojević, R. M. Thorne, and R. B. Horne (2014), Electromagnetic ion cyclotron wave modeling during the geospace environment modeling challenge event, *J. Geophys. Res. Space Physics*, *119*, 2963–2977, doi:10.1002/2013JA019595.

Cornwall, J. M. (1965), Cyclotron instabilities and electromagnetic emission in the ultra low frequency and very low frequency ranges, *J. Geophys. Res.*, *70*(1), 61–69, doi:10.1029/JZ070i001p00061.

Cornwall, J. M., F. V. Coroniti, and R. M. Thorne (1970), Turbulent loss of ring current protons, *J. Geophys. Res.*, *75*(25), 4699–4709, doi:10.1029/JA075i025p04699.

Denton, R. E. (2006), Magneto-seismology using spacecraft observations, in *Magnetospheric ULF Waves: Synthesis and New Directions, Geophys. Monogr. Ser. 169*, edited by K. Takahashi et al., pp. 307–317, AGU, Washington, D. C.

Denton, R. E., M. K. Hudson, S. A. Fuselier, and B. J. Anderson (1993), Electromagnetic ion cyclotron waves in the plasma depletion layer, *J. Geophys. Res.*, *98*(A8), 13,477–13,490, doi:10.1029/93JA00796.

Denton, R. E., V. K. Jordanova, and B. J. Fraser (2014), Effect of spatial density variation and O+ concentration on the growth and evolution of electromagnetic ion cyclotron waves, *J. Geophys. Res. Space Physics*, *119*, 8372–8395, doi:10.1002/2014JA020384.

Fraser, B. J., H. J. Singer, M. L. Adrian, D. L. Gallagher, and M. F. Thomsen (2005), The relationship between plasma density structure and EMIC waves at geosynchronous orbit, in *Inner Magnetosphere Interactions: New Perspectives From Imaging*, edited by J. Burch, M. Schulz, and H. Spence, pp. 55–70, AGU, Washington, D. C., doi:10.1029/159GM04.

Fu, X., et al. (2014), Whistler anisotropy instabilities as the source of banded chorus: Van Allen Probes observations and particle-in-cell simulations, *J. Geophys. Res. Space Physics*, *119*, 8288–8298, doi:10.1002/2014JA020364.

Funsten, H., et al. (2013), Helium, oxygen, proton, and electron (HOPE) mass spectrometer for the radiation belt storm probes mission, *Space Sci. Rev.*, *179*(1–4), 423–484, doi:10.1007/s11214-013-9968-7.

Gary, S. P., and M. A. Lee (1994), The ion cyclotron anisotropy instability and the inverse correlation between proton anisotropy and proton beta, *J. Geophys. Res.*, *99*(A6), 11,297–11,301, doi:10.1029/94JA00253.

Gary, S. P., K. Liu, and L. Chen (2012), Alfvén-cyclotron instability with singly ionized helium: Linear theory, *J. Geophys. Res.*, *117*, A08201, doi:10.1029/2012JA017740.

Goldstein, J., M. F. Thomsen, and A. DeJong (2014a), In situ signatures of residual plasmaspheric plumes: Observations and simulation, *J. Geophys. Res. Space Physics*, *119*, 4706–4722, doi:10.1002/2014JA019953.

Goldstein, J., S. D. Pascuale, C. Kletzing, W. Kurth, K. J. Genestreti, R. M. Skoug, B. A. Larsen, L. M. Kistler, C. Mouikis, and H. Spence (2014b), Simulation of Van Allen Probes plasmapause encounters, *J. Geophys. Res. Space Physics*, *119*, 7464–7484, doi:10.1002/2014JA020252.

Gomberoff, L., and R. Neira (1983), Convective growth rate of ion cyclotron waves in a H^+/He^+ and $H^+/He^{++}/O^+$ plasma, *J. Geophys. Res.*, *88*, 2170–2174, doi:10.1029/JA088iA03p02170.

Horne, R., and R. Thorne (1994), Convective instabilities of electromagnetic ion cyclotron waves in the outer magnetosphere, *J. Geophys. Res.*, *99*(A9), 17,259–17,273, doi:10.1029/94JA01259.

Horne, R. B., and R. M. Thorne (1993), On the preferred source location for the convective amplification of ion cyclotron waves, *J. Geophys. Res.*, *98*(A6), 9233–9247, doi:10.1029/92JA02972.

Horne, R. B., and R. M. Thorne (1997), Wave heating of He^+ by electromagnetic ion cyclotron waves in the magnetosphere: Heating near the H^+-He^+ bi-ion resonance frequency, *J. Geophys. Res.*, *102*(A6), 11,457–11,471, doi:10.1029/97JA00749.

Hu, Y., and R. E. Denton (2009), Two-dimensional hybrid code simulation of electromagnetic ion cyclotron waves in a dipole magnetic field, *J. Geophys. Res.*, *114*, A12217, doi:10.1029/2009JA014570.

Hu, Y., R. E. Denton, and J. R. Johnson (2010), Two-dimensional hybrid code simulation of electromagnetic ion cyclotron waves of multi-ion plasmas in a dipole magnetic field, *J. Geophys. Res.*, *115*, A09218, doi:10.1029/2009JA015158.

Jordanova, V. K., C. J. Farrugia, R. M. Thorne, G. V. Khazanov, G. D. Reeves, and M. F. Thomsen (2001), Modeling ring current proton precipitation by electromagnetic ion cyclotron waves during the May 14–16, 1997, storm, *J. Geophys. Res.*, *106*(A1), 7–22, doi:10.1029/2000JA002008.

Kennel, C. F., and H. E. Petschek (1966), Limit on stably trapped particle fluxes, *J. Geophys. Res.*, *71*(1), 1–28, doi:10.1029/JZ071i001p00001.

Kessel, R., N. Fox, and M. Weiss (2012), The radiation belt storm probes (RBSP) and space weather, *Space Sci. Rev.*, *179*, 531–543, doi:10.1007/s11214-012-9953-6.

Khazanov, G. V., K. V. Gamayunov, D. L. Gallagher, and J. U. Kozyra (2006), Self-consistent model of magnetospheric ring current and propagating electromagnetic ion cyclotron waves: Waves in multi-ion magnetosphere, *J. Geophys. Res.*, *111*, A10202, doi:10.1029/2006JA011833.

Kletzing, C., et al. (2013), The Electric and Magnetic Field Instrument Suite and Integrated Science (EMFISIS) on RBSP, *Space Sci. Rev.*, *179*, 127–181, doi:10.1007/s11214-013-9993-6.

Kozyra, J. U., T. E. Cravens, A. F. Nagy, E. G. Fontheim, and R. S. B. Ong (1984), Effects of energetic heavy ions on electromagnetic ion cyclotron wave generation in the plasmapause region, *J. Geophys. Res.*, *89*(A4), 2217–2233, doi:10.1029/JA089iA04p02217.

Lee, J. H., and V. Angelopoulos (2014), On the presence and properties of cold ions near Earth's equatorial magnetosphere, *J. Geophys. Res. Space Physics*, *119*, 1749–1770, doi:10.1002/2013JA019305.

Lee, J. H., L. Chen, V. Angelopoulos, and R. M. Thorne (2012), THEMIS observations and modeling of multiple ion species and EMIC waves: Implications for a vanishing He^+ stop band, *J. Geophys. Res.*, *117*, A06204, doi:10.1029/2012JA017539.

Liu, K., D. S. Lemons, D. Winske, and S. P. Gary (2010), Relativistic electron scattering by electromagnetic ion cyclotron fluctuations: Test particle simulations, *J. Geophys. Res.*, *115*, A04204, doi:10.1029/2009JA014807.

MacDonald, E., M. Denton, M. Thomsen, and S. Gary (2008), Superposed epoch analysis of a whistler instability criterion at geosynchronous orbit during geomagnetic storms, *J. Atmos. Sol. Terr. Phys.*, *70*(14), 1789–1796, doi:10.1016/j.jastp.2008.03.021.

Matsuda, S., Y. Kasahara, and Y. Goto (2014), Electromagnetic ion cyclotron waves suggesting minor ion existence in the inner magnetosphere observed by the Akebono satellite, *J. Geophys. Res. Space Physics*, *119*, 4348–4357, doi:10.1002/2013JA019370.

Mauk, B. H., N. J. Fox, S. G. Kanekal, R. L. Kessel, D. G. Sibeck, and A. Ukhorskiy (2012), Science objectives and rationale for the radiation belt storm probes mission, *Space Sci. Rev.*, *179*, 3–27, doi:10.1007/s11214-012-9908-y.

Millan, R. M., and R. M. Thorne (2007), Review of radiation belt relativistic electron losses, *J. Atmos. Sol. Terr. Phys.*, *69*(3), 362–377, doi:10.1016/j.jastp.2006.06.019.

Omidi, N., R. M. Thorne, and J. Bortnik (2010), Nonlinear evolution of EMIC waves in a uniform magnetic field: 1. Hybrid simulations, *J. Geophys. Res.*, *115*, A12241, doi:10.1029/2010JA015607.

Omidi, N., J. Bortnik, R. Thorne, and L. Chen (2013), Impact of cold O^+ ions on the generation and evolution of EMIC waves, *J. Geophys. Res. Space Physics*, *118*, 434–445, doi:10.1029/2012JA018319.

Perraut, S., R. Gendrin, and A. Roux (1976), Amplification of ion-cyclotron waves for various typical radial profiles of magnetospheric parameters, *J. Atmos. Terr. Phys.*, *38*(11), 1191–1199, doi:10.1016/0021-9169(76)90051-9.

Sakaguchi, K., Y. Kasahara, M. Shoji, Y. Omura, Y. Miyoshi, T. Nagatsuma, A. Kumamoto, and A. Matsuoka (2013), Akebono observations of EMIC waves in the slot region of the radiation belts, *Geophys. Res. Lett.*, *40*, 5587–5591, doi:10.1002/2013GL058258.

Santolík, O., M. Parrot, and F. Lefeuvre (2003), Singular value decomposition methods for wave propagation analysis, *Radio Sci.*, *38*(1), 1010, doi:10.1029/2000RS002523.

Shprits, Y. Y., D. Subbotin, A. Drozdov, M. E. Usanova, A. Kellerman, K. Orlova, D. N. Baker, D. L. Turner, and K.-C. Kim (2013), Unusual stable trapping of the ultrarelativistic electrons in the Van Allen radiation belts, *Nat. Phys.*, *9*, 699–703, doi:10.1038/nphys2760.

Silin, I., I. R. Mann, R. D. Sydora, D. Summers, and R. L. Mace (2011), Warm plasma effects on electromagnetic ion cyclotron wave MeV electron interactions in the magnetosphere, *J. Geophys. Res.*, *116*, A05215, doi:10.1029/2010JA016398.

Spence, H., et al. (2013), Science Goals and Overview of the Radiation Belt Storm Probes (RBSP) Energetic Particle, Composition, and Thermal Plasma (ECT) Suite on NASA's Van Allen Probes Mission, *Space Sci. Rev.*, *179*(1–4), 311–336, doi:10.1007/s11214-013-0007-5.

Summers, D., and R. M. Thorne (2003), Relativistic electron pitch-angle scattering by electromagnetic ion cyclotron waves during geomagnetic storms, *J. Geophys. Res.*, *108*(A4), 1143, doi:10.1029/2002JA009489.

Thorne, R. M., and R. Horne (1997), Modulation of electromagnetic ion cyclotron instability due to interaction with ring current O^+ during magnetic storms, *J. Geophys. Res.*, *102*(A7), 14,155–14,163, doi:10.1029/96JA04019.

Thorne, R. M., and R. B. Horne (1993), Cyclotron absorption of ion-cyclotron waves at the bi-ion frequency, *Geophys. Res. Lett.*, *20*(4), 317–320, doi:10.1029/93GL00089.

Thorne, R. M., and R. B. Horne (1994), Energy transfer between energetic ring current H^+ and O^+ by electromagnetic ion cyclotron waves, *J. Geophys. Res.*, *99*(A9), 17,275–17,282, doi:10.1029/94JA01007.

Thorne, R. M., R. B. Horne, V. K. Jordanova, J. Bortnik, and S. Glauert (2006), Interaction of EMIC waves with thermal plasma and radiation belt particles, in *Magnetospheric ULF Waves: Synthesis and New Directions*, edited by K. Takahashi et al., pp. 213–223, AGU, Washington, D. C., doi:10.1029/169GM14.

Winske, D., and N. Omidi (1993), *Hybrid Codes: Methods and Applications*, pp. 103–160, Terra Sci., Tokyo.

Wygant, J., et al. (2013), The electric field and waves instruments on the radiation belt storm probes mission, *Space Sci. Rev.*, *179*(1–4), 183–220, doi:10.1007/s11214-013-0013-7.

Zhang, J.-C., L. M. Kistler, C. G. Mouikis, M. W. Dunlop, B. Klecker, and J.-A. Sauvaud (2010), A case study of EMIC wave-associated He^+ energization in the outer magnetosphere: Cluster and Double Star 1 observations, *J. Geophys. Res.*, *115*, A06212, doi:10.1029/2009JA014784.

Zhang, J.-C., et al. (2014), Excitation of EMIC waves detected by the Van Allen Probes on 28 April 2013, *Geophys. Res. Lett.*, *41*, 4101–4108, doi:10.1002/2014GL060621.